



Atomic layer deposition of nanometric alumina for corrosion protection of heterogeneous metallic surfaces – The case of aeronautical grade aluminium alloy 2024-T3

Marco P. Oliveira^a, Ricardo M. Silva^a, Kiryl A. Yasakau^a, Alexandre Bastos^{a,*}, Silvar Kallip^b, Mikhail L. Zheludkevich^{c,d}, Rui F. Silva^a, Mário G.S. Ferreira^a

^a CICECO - Aveiro Institute of Materials and DEMaC - Department of Materials and Ceramic Engineering, University of Aveiro, 3810-193 Aveiro, Portugal

^b Institute of Chemistry, University of Tartu, 50411 Tartu, Estonia

^c Institute of Surface Science, Helmholtz-Zentrum Hereon, Geesthacht 21502, Germany

^d Institute for Materials Science, Faculty of Engineering, Kiel University, Kiel 24103, Germany

ARTICLE INFO

Keywords:

- A. alloy
- A. aluminium
- B. AFM
- B. EIS
- B. polarization
- C. Passive films

ABSTRACT

Nanometric layers of Al₂O₃ were applied by atomic layer deposition (ALD) on 2024-T3 aluminium alloy. The ALD layers suppressed the corrosion of the alloy as confirmed by Scanning Kelvin Probe Force Microscopy (SKPFM), polarization curves and Electrochemical Impedance Spectroscopy (EIS). The protection provided by the ALD layers weakened with the time of immersion and this was attributed to the incorporation of hydroxyl species in the film during the deposition at low temperature (100 °C) making them vulnerable to water.

1. Introduction

After the iron-based alloys, aluminium alloys are the second most used in the world, being preferred for many applications due to the lightweight and corrosion resistance [1]. Their surface is spontaneously covered by a layer of aluminium oxide of about 3–4 nm that protects them from corrosion [1,2]. Aluminium alloys are classified according to the main alloying element, which determines to a large extent their mechanical properties [3]. The 2000 series have copper as the main alloying element and are used in applications requiring high specific strength. A typical example is aluminium alloy 2024 with a particular heat treatment (AA2024-T3), commonly used in the aircraft industry [4]. The heat treatment increases the strength of the alloy by forming a high density of nanometre size precipitates like Guinier–Preston–Bagaryatsky (GPB) zones, and S-phase precipitates (Al₂CuMg) [5, 6]. Coarse intermetallic particles (Al₂CuMg, Al-Cu-Fe-Mn) are formed during the solidification. The particles at the surface give rise to micro-galvanic couples with the aluminium matrix that significantly decrease the corrosion resistance of the alloy [7,8]. This is one of the main drawbacks of most aluminium alloys and a challenging topic within the corrosion research community.

The protection of AA2024-T3 against corrosion has been provided by either, a thin film of pure aluminium (cladding), an alumina layer produced by the anodizing process, an organic coating (paint), or a combination of them [8,9]. These layers function as a protective barrier separating the metal from the environment. An alumina layer can also be produced by other methods like physical vapor deposition (PVD) [10] and chemical vapor deposition (CVD) [11]. A variant of CVD is atomic layer deposition (ALD) in which two chemical reactants (precursors) are separately fed into the reactor where they react with the surface in self-terminated reactions. The independent reaction of each precursor and the inert gas purge between them correspond to one reaction cycle. The number of cycles determines the thickness of the layer.

This process can produce thin films of a wide range of materials, with high conformability, even in substrates with complex geometries [12, 13]. ALD has been applied in many research fields, such as the production of silicon wafer semiconductors [14], energy conversion and storage materials like solid oxide fuel cells [15], supercapacitors [16], solar cells [17], optoelectronics [18,19], and catalysis [20–22]. ALD has also been explored for the corrosion protection of metals and alloys. For example, Al₂O₃ and Ta₂O₅ films deposited by ALD have been tested for the protection of carbon/low alloy steel [23–25] and 316L stainless steel

* Corresponding author.

E-mail address: acbastos@ua.pt (A. Bastos).

<https://doi.org/10.1016/j.corsci.2022.110773>

Received 6 May 2022; Received in revised form 17 October 2022; Accepted 19 October 2022

Available online 22 October 2022

0010-938X/© 2022 Elsevier Ltd. All rights reserved.

[26,27]. Films of ZrO_2 were tested in magnesium alloys, and copper was coated with Al_2O_3 , TiO_2 , ZnO , HfO_2 and ZnO_2 [28,29]. Nanolaminates of TiO_2/Al_2O_3 have also been used to seal the pores of anodized AA2024 [30]. In general, these works showed the formation of thin films (10–100 nm) with high conformability and uniformity, without pinholes or other defects. Films with less than 10 nm could present some porosity but it decreased rapidly with increasing thickness [23,27,29]. The best sealing properties were achieved with Al_2O_3 [24,29].

In these past studies, the ALD layers were applied on pure metals or homogeneous alloys. This work investigates the suitability of using ALD to produce a continuous and adherent layer of Al_2O_3 on AA2024-T3 with the aim to entirely cover aluminium matrix and the intermetallic particles. The motivation is to increase the resistance to corrosion by minimising the propensity to micro-galvanic coupling. The concept is schematically illustrated in Fig. 1. In the ALD process followed here, a cycle for producing a single layer of Al_2O_3 involves the reaction between trimethylaluminum ($Al(CH_3)_3$) and water (H_2O) (Fig. 2). The cycle is repeated until the deposited film reaches the desired thickness [12,31,32]. Three films with thicknesses of 5 nm, 15 nm and 50 nm, were produced by adjusting the number of ALD cycles. The process occurred at low temperature (100 °C) to minimize its effect on the mechanical properties of AA2024 [33,34].

The ALD coated samples were immersed in near neutral 0.05 M NaCl aqueous solution and the corrosion resistance was assessed by polarization curves/linear sweep voltammetry (LSV), electrochemical impedance spectroscopy (EIS), and scanning vibrating electrode technique (SVET). The surface was also analysed by scanning Kelvin probe force microscopy, atomic force microscopy (AFM) and scanning electron microscopy (SEM).

2. Experimental

2.1. Material

The metal substrate was aluminium alloy 2024-T3 sheet with a nominal composition (in weight) of: Cu 3.8–4.9 %, Fe 0.5 %, Cr 0.1 %, Mg 1.2–1.8 %, Mn 0.3–0.9 %, Si 0.5 %, Ti 0.15 %, Zn 0.25 %, others 0.15 % and Al balance. The thickness of the sheet was 1 mm.

2.2. Sample preparation

AA2024-T3 sheet was cut in square pieces of $2.0 \times 2.0 \text{ cm}^2$ and the surface abraded with SiC paper (Buehler) from P600 to P4000 grades with ethanol as a lubricant. Samples for SKPFM were further polished with alumina suspensions (see below). Subsequently the samples were sonicated in ethanol. To minimize the surface oxidation and contamination, they remained immersed in ethanol while being transported to the ALD deposition room, where they were finally dried with a stream of N_2 , before entering the chamber.

2.3. Atomic layer deposition (ALD) of Al_2O_3

Alumina (Al_2O_3) thin films were deposited on AA2024-T3. The specimens were introduced in a homemade crossflow thermal ALD reactor, working in exposure mode at 100 °C (heating element controlled by a K-type thermocouple). The trimethylaluminum (TMA, 97 % purity, Sigma-

Aldrich) and ultrapure water (UP, MiliQ, H_2O) precursors were introduced into the reaction chamber in a sequence using pure nitrogen (N_2) as purging and as carrier gas. One ALD cycle was performed in a sequence of pulse/exposure/ N_2 -purging of 0.5 s/30 s/30 s for TMA and 1.0 s/20 s/30 s for H_2O . The precursor pulsing was made with N_2 flow rate of 100 sccm and the pressure was 1.8 Torr before and 2.0 Torr after the pulsing. N_2 purging with the same flow rate was used to remove by-products and unreacted precursor from the ALD chamber between cycles. The deposition parameters were chosen according to the reported in the literature [32]. Samples with thicknesses of ~ 5, 15 and 50 nm were prepared by adjusting the number of ALD cycles (respectively 50, 100 and 400 cycles).

2.4. Scanning electron microscopy (SEM)

The samples morphology was characterized via scanning electron microscopy using a Hitachi SU-70 Schottky emission scanning electron microscope with an electron beam energy of 15 kV.

2.5. Atomic force microscopy (AFM) and Scanning Kelvin probe force microscopy (SKPFM)

For the AFM/SKPFM measurements, the bare AA2024-T3 samples were further polished with alumina suspensions (Struers AP-D suspensions) of 100 nm and 10 nm and sonicated in ethanol before entering in the ALD chamber. A Digital Instruments NanoScope III atomic force microscope equipped with Extender™ Electronic Module was used for measurements. Volta potential difference (VPD) maps were acquired at lift height 100 nm and ac voltage bias of 5 V applied to the tip. Silicon probes covered with Cr/Pt layers purchased from BudgetSensors were used. Moreover, a Ni reference was used to check the values of the AFM probes ensuring that the VPD measurements are consistent. The measurements were carried out at a temperature about 24 °C and relative humidity $52 \pm 2 \%$. The data was levelled by moving the mean value to zero and the reported VPD values are referenced versus the levels of aluminium matrixes. Positive values represent noble zones, while negative values represent less noble zones. More details on the technique and interpretation of results are given in other publications [35–39].

2.6. Polarization curves/linear sweep voltammetry (LSV)

Polymethylmethacrylate (PMMA) tubes with 16 mm diameter were glued to each sample surface with epoxy cement, leaving an exposed area of 2 cm^2 . A three-electrode electrochemical cell was assembled with the exposed sample area as working electrode, a saturated calomel electrode (SCE) as reference and a platinum wire as counter electrode. Aqueous 0.05 M NaCl solution, prepared with NaCl (99.5 %, Fluka) and distilled water, was used as testing medium.

Polarization curves (linear staircase potential sweep) were measured with an Autolab 302 N potentiostat/galvanostat and the GPES 4.8 software, after 30 min of immersion and after ensuring a near stable sample potential. Independent anodic and cathodic sweeps were measured with new samples, with a scan rate of 1 mV s^{-1} . The anodic polarizations started at OCP-10 mV (OCP is open circuit potential) and continued until a current increase of several orders of magnitude was registered. The cathodic sweeps started at OCP + 10 mV and terminated at $-1.5 V_{SCE}$.

2.7. Electrochemical Impedance Spectroscopy (EIS)

EIS measurements were performed with a Autolab PGSTAT204 potentiostat and the Nova 2 software. The experimental cell set-up was the same as described for the polarization curves. The spectra were collected at various times of immersion (30 min, 3 h, 6 h, 12 h, 24 h and 48 h) from 100 kHz to 1 MHz, with 7 points per decade with a sinusoidal

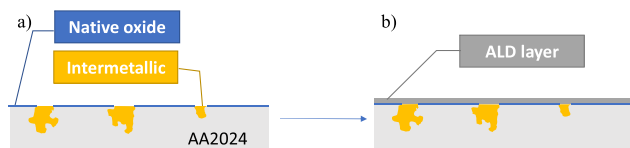


Fig. 1. a) AA2024-T3 surface with intermetallic particles and b) the blocking effect of the Al_2O_3 layer deposited by ALD. Sketch not to scale.

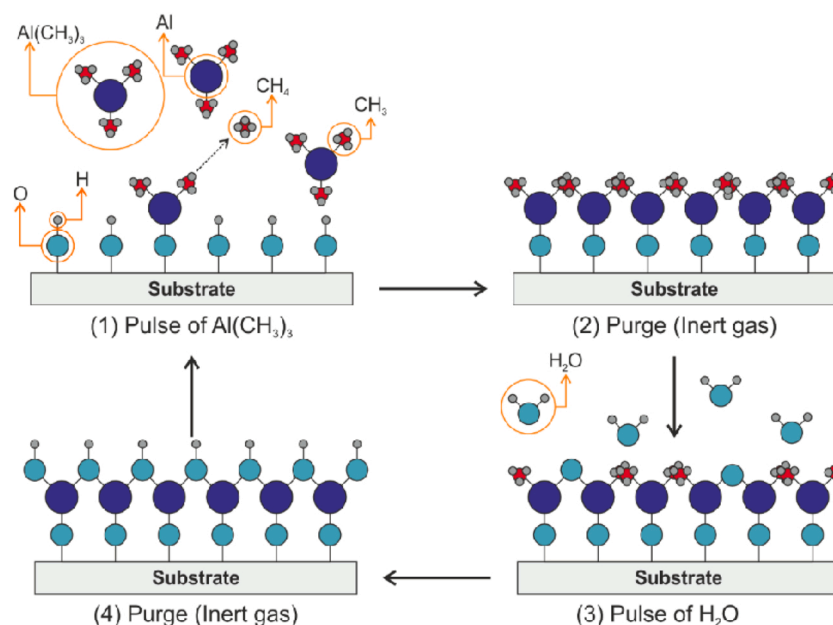


Fig. 2. Illustration of the ALD cycle for producing a single layer of Al_2O_3 from $\text{Al}(\text{CH}_3)_3$ and H_2O precursors.

perturbation of 10 mV rms around OCP. The EIS spectra were fitted with ZView 3.5i software (Scribner Associates, USA).

2.8. Scanning vibrating electrode technique (SVET)

After the EIS measurements, some parts of the samples were analysed by the Scanning Vibrating Electrode Technique (SVET) [40]. The selected regions were cut and glued in an epoxy holder. The surfaces were isolated with a mixture of beeswax and colophony (3:1 in mass proportion) except for the areas to be mapped. The SVET equipment was manufactured by Applicable Electronics Inc. (USA) [41] and was controlled by the ASET program developed by Science Wares Inc. (USA) [42]. The vibrating microelectrode was a 250 μm diameter and 1.5 cm long platinum-iridium wire, covered by insulating parylene C® polymer, and thinned at the end to a tip of $\sim 3 \mu\text{m}$ (Microprobes Inc, USA [43]). Only the tip of the microelectrode was electroactive and a platinum black deposit of 20 μm was grown on it, to increase sensitivity. Each scan comprised 40×40 points and was measured at an average distance of 100 μm from the surface. The time acquisition in each point was 0.02 s. The microelectrode vibrated with a frequency of 89 Hz and 10 μm amplitude in the direction normal to the surface.

3. Results and discussion

3.1. Surface morphology

Fig. 3 shows SEM pictures of the AA2024-T3 surface covered with the 50 nm alumina film. The bright spots are the intermetallic particles, which play a crucial role on the corrosion of this alloy, becoming local cathodes or local anodes, depending on the nature of the particle [7,44]. Blisters and defects like those observed before in ALD films applied on copper [45] were not detected even at higher magnification – Fig. 3(b). Similar Al_2O_3 films were applied with the same deposition conditions to PET plastic [32], boron doped diamond [46] and stainless steels [47]. More information about the film properties can be found there.

3.2. SKPFM/AFM

Fig. 4 depicts topography and Volta potential maps of areas of the alloy containing S-phase intermetallic particles (Al_2CuMg). The

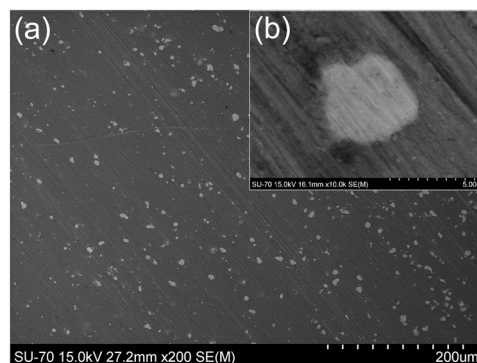


Fig. 3. a) SEM micrograph of the AA2024-T3 surface with a 50 nm Al_2O_3 film deposited by ALD, b) detailed view of one intermetallic particle.

topography is generally uniform except on the S-phase particles that were over polished due to the different hardness. The S-phase shows a VPD higher than the Al-based matrix. This is attributed to the preferential attack at the top of the particles by the polishing process using the alumina-based suspensions that makes the particles nobler than the Al matrix [48,49]. Similarly, the Al-Fe-Mn intermetallic also shows a higher VPD (see Supporting information). The potential maps of the bare substrate display numerous small spots of high VPD (bright places). Such spots are assigned to the various small intermetallics and dispersoids that contribute to the microstructure of the alloy [7].

After the ALD process, the maps display a much smaller potential difference between the S-phase particles and the matrix. Most of the smaller dispersoids are no longer detectable. The thicker the film, the less is the contrast (or VPD offset) between the S-phases and matrix displayed on the VPD maps. This is explained by the insulating Al_2O_3 film that “screens” the VPD [50] and diminishes the potential difference between the S-phase particles and the matrix. Fig. 5 supports this assumption, as it shows that VPD changes across the S-phase intermetallics become closer to the VPD of the aluminium matrix on the profiles after the ALD treatment compared with those before the treatment. The effects are more pronounced on the thicker ALD film (Figs. 4 and 5) but do not seem to be linearly dependent on the layer thickness (Fig. 5). At the thicknesses of 5 nm and 15 nm the VPD offsets are

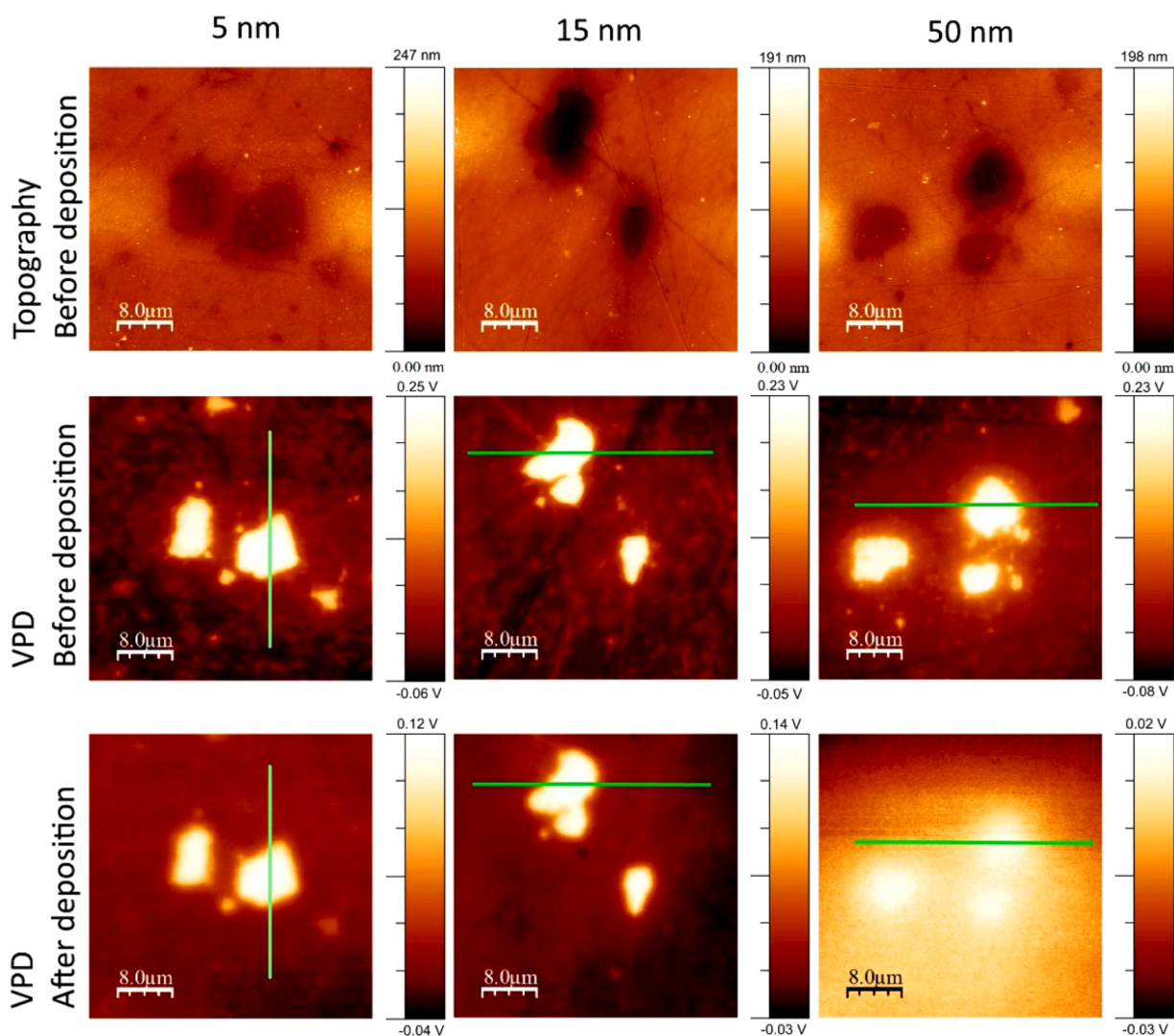


Fig. 4. Topography before deposition of different samples of AA2024-T3 containing S-phase particles that were after covered with Al_2O_3 films of different thicknesses and respective Volta potential difference maps before and after film deposition (5 nm, 15 nm, 20 nm). VPD profiles along the green lines are presented in Fig. 5.

similar, and at 50 nm films the offset is barely visible. Since the ALD process forms consistent, conformal coatings with the same composition, there might be changes at the matrix(intermetallic)/ALD coating interface that contribute to the measured VPD. The semiconductive properties at the interface and electronic defects are considered contributing factors to the measured VPD [51]. In this study it was not possible to unambiguously identify which parameter is responsible for the VPD changes on the ALD coated samples. In any case the ALD films, particularly the thicker one, were able to significantly decrease the potential difference between particles and matrix, thus reducing the risk of micro-galvanic corrosion. The insulating character of the Al_2O_3 layer also contributes to the lower susceptibility to corrosion of the coated samples.

3.3. Polarization curves

Despite their thinness, the ALD films were able to influence the electrochemical response of AA2024-T3. The polarisation curve of the bare substrate presented in Fig. 6 (in black) shows a rapid increase in the anodic current upon a positive potential shift from the corrosion potential indicating no spontaneous passivity, and pitting initiation near the corrosion potential. The potential sweep in the negative direction

presents a region of potential-independent current corresponding to the diffusion-limited reduction of dissolved oxygen followed by an increase in current for potentials more negative than $-1 \text{ V}_{\text{SCE}}$ due the water reduction. The 5 nm ALD film has a minor effect on the anodic breakdown potential although decreasing the cathodic current by one order of magnitude. The barrier effect is pronounced only in films of 15 and 50 nm which show negligible currents (coincident with the lower measuring limit of the potentiostat) in a wide potential window. The reduction reactions were delayed until $-1.3 \text{ V}_{\text{SCE}}$, revealing the insulating character of the ALD alumina layer for the conduction of both ions and electrons. The oxidation of the substrate was prevented until potentials of $0.3 \text{ V}_{\text{SCE}}$ for 15 nm and $0.9 \text{ V}_{\text{SCE}}$ for 50 nm (in some samples the breakdown potential was up to 6 V_{SCE}). Nevertheless, the values are far from the 7.5 and 35 V expected for films of 15 and 50 nm thicknesses, respectively, considering the typical values of 0.5–0.7 V/nm for the breakdown voltage of perfect alumina films [52].

After the anodic polarization the samples with 15 or 50 nm ALD film showed just a few pits with the rest of the surface remaining intact. Fig. 7a) shows the surface of a sample with 50 nm film, in pristine condition except for 3 pits. Magnification of one of the pits reveals the ALD film with metal dissolution underneath – Fig. 7b).

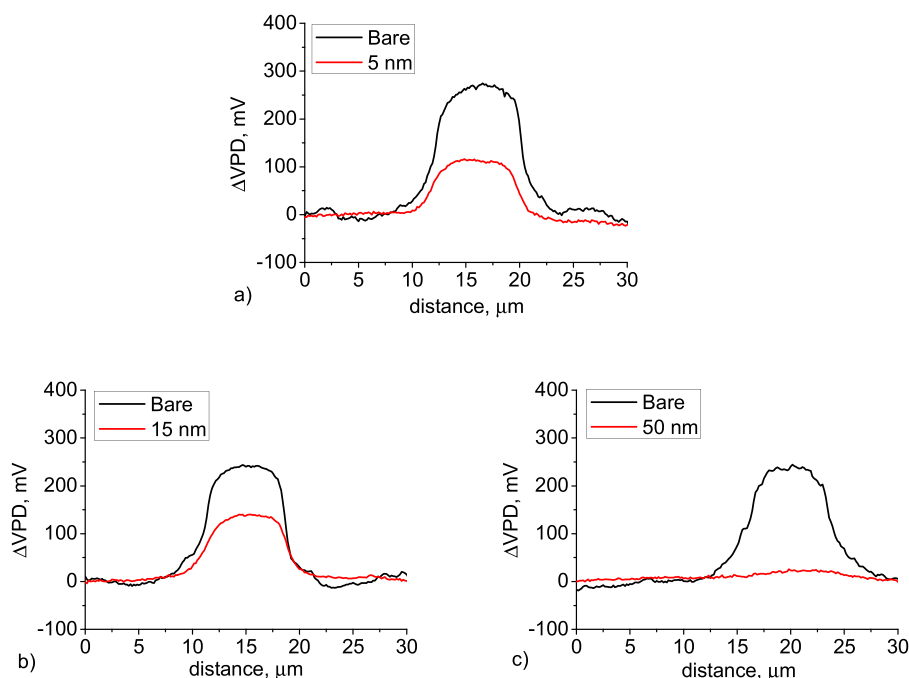


Fig. 5. VPD profiles of the surface containing S-phase intermetallics measured in the lines shown in Fig. 4, profiles of the sample with 5 nm a), 15 nm b) and 50 nm c) before (black) and after ALD film (green).

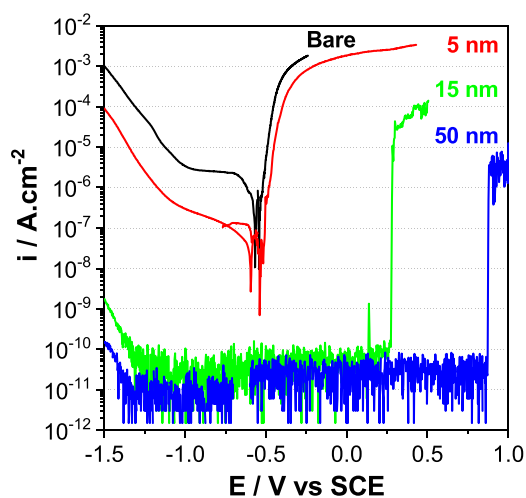


Fig. 6. Anodic and cathodic polarization plots of AA2024 in bare condition and with alumina films of 5, 15 and 50 nm thickness deposited by ALD.

3.4. Electrochemical impedance spectroscopy (EIS)

The effect of immersion time on the barrier properties of the deposited layers was studied using EIS. The results are presented in Fig. 8 in the form of Bode plots. The bare 2024-T3 aluminium alloy showed a response that practically did not change over time, with low impedance values and two relaxation processes, one attributed to the double layer capacitance + charge transfer resistance and the other, at lower frequencies, to diffusion [53]. The impedance of the coated systems was 3–4 orders of magnitude higher at the beginning of the immersion and was dominated by a capacitive response in a wide range of frequencies. This response was assigned to the ALD layer [23,26] which works as a dielectric material between two conductive surfaces, the metal on one side and the electrolytic solution on the other side, hence the capacitive response. Then, as immersion time elapsed, the impedance dropped, and new relaxation processes appeared in the spectra. The

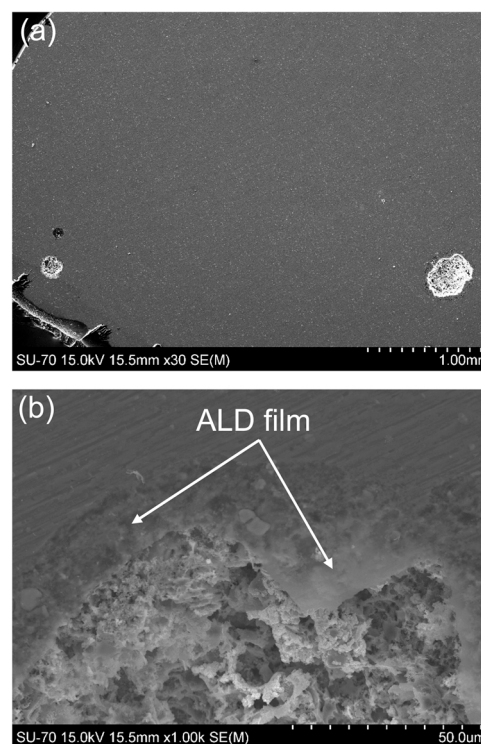


Fig. 7. a) SEM micrograph of the sample with 50 nm Al_2O_3 film after anodic polarization and b) a close-up of one pit with the ALD films and metal dissolution underneath.

drop in impedance reflects the appearance of conductive pathways through the dielectric (ALD) barrier. The new relaxation processes are associated with the corrosion that starts at the metal substrate once it becomes in contact with the solution at the bottom of the conductive pathways.

The decrease in impedance was more significant in the sample with

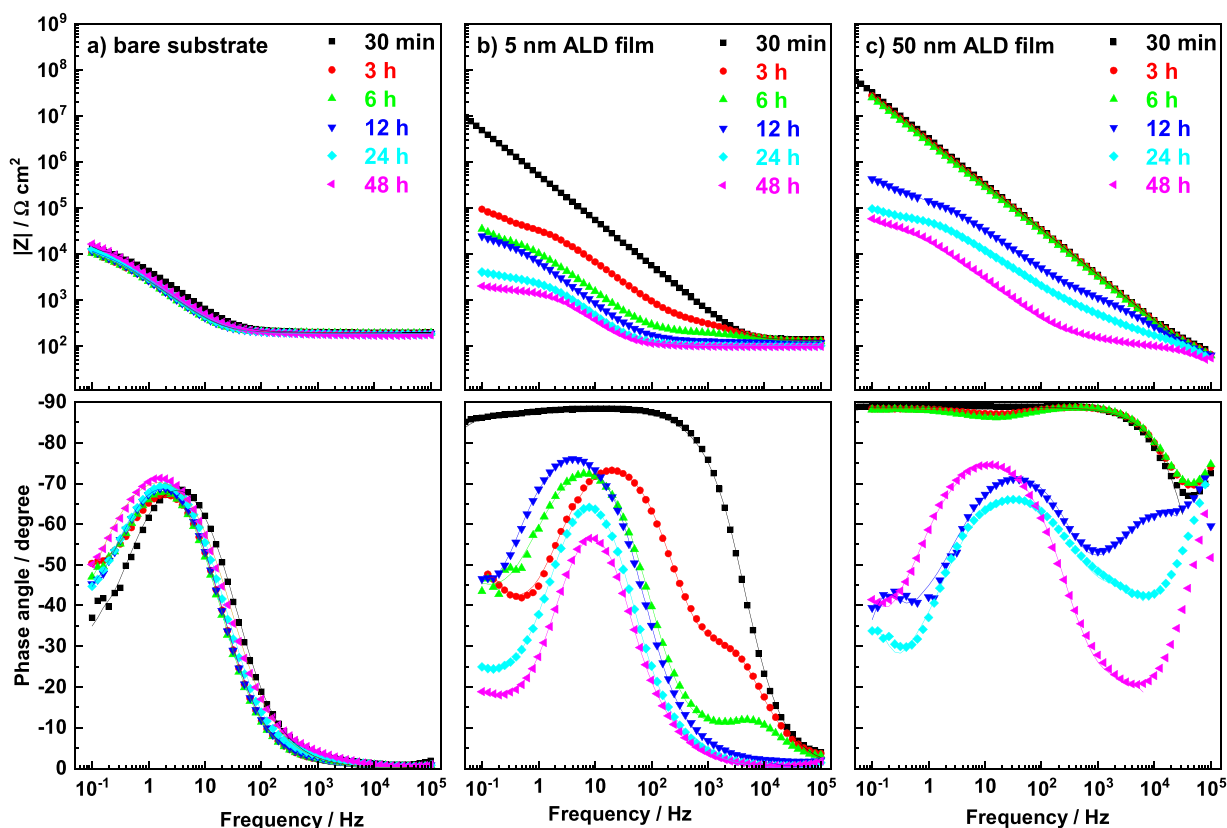


Fig. 8. Impedance response (Bode plots) of a) bare AA2024-T3, b) AA2024-T3 surface with 5 nm ALD film, c) surface with 50 nm ALD film, during immersion in 0.05 M NaCl (symbols are experimental points and lines refer to fitted response).

the 5 nm layer. After 48 h of immersion the impedance response became close to that of the bare substrate. On the samples with thicker layers the impedance was higher and remained higher for longer time. Fig. 8c) shows the results of the sample with 50 nm ALD layer. The sample with 15 nm ALD layer presented similar response and therefore is not shown.

The experimental results were numerically fitted with the circuits presented in Fig. 9, where R_{sol} is the uncompensated solution resistance, CPE_{dl} represents the double layer capacitance, R_{ct} is the charge transfer resistance, W is the diffusion impedance, CPE_{film} represents the capacitance of the ALD film, and R_{pore} is the resistance of the electrolyte inside the pores of the film. Circuit 9 a) was used for the bare AA2024 surface [53], circuit 9 b) was used for intact ALD films [23,26] and circuit 9c) was used when defects and corrosion appeared in the coated samples [29]. In the fitting procedure, constant phase elements (CPE) were used instead of pure capacitances because real systems do not show ideal

single-valued time constants, rather time-constant dispersions [54], and CPE is a simple and common way to numerically account for this dispersion. The capacitances were estimated from the CPEs using the Brug's formula [55]. The fitted results correspond to the lines in Fig. 8 while the points are experimental data. Fig. 10 shows the evolution of the fit parameters with the time of immersion, with further fitting parameters shown in Table S1. The highest C_{dl} and lowest R_{ct} were found on the bare AA2024-T3. The values remained nearly constant over the testing period. The impedance of the ALD coated samples was very high at the beginning of the immersion. The response was capacitive, with small C_{film} . After a few hours R_{pore} started being measured which means that the electrolyte ions entered the film and facilitated the passage of electric signal across it. The decrease of R_{pore} signifies an increasing number and/or size of pores. Pores here denote any means by which electric charges can pass across the ALD layer. The barrier properties of

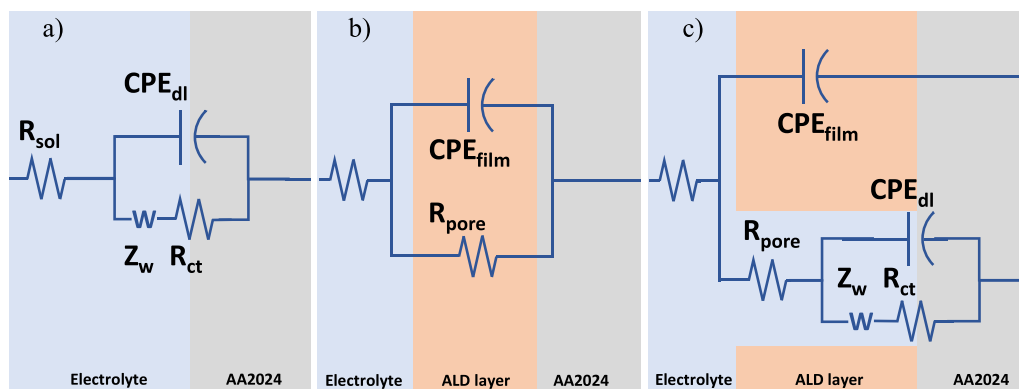


Fig. 9. Equivalent circuits used to fit the impedance data, a) uncoated surface, b) intact ALD film and c) film with defects and corrosion.

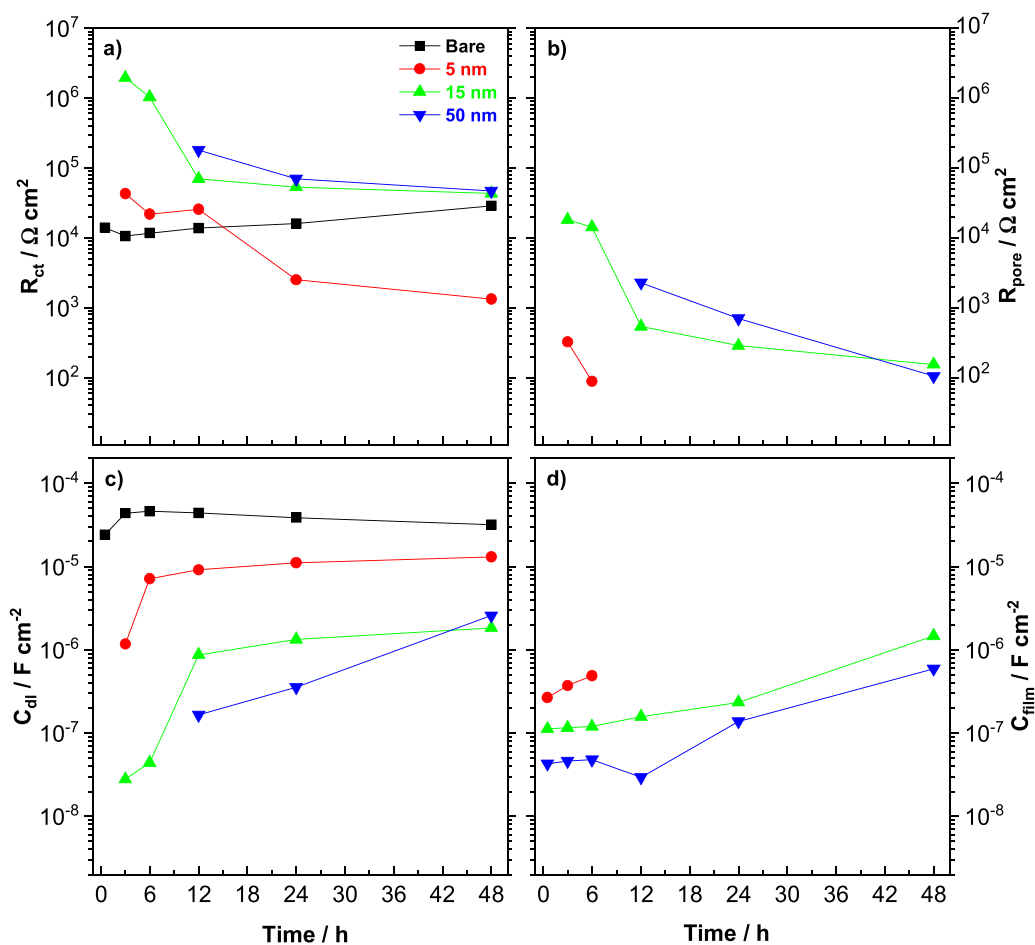


Fig. 10. Time evolution of the fitted parameters: a) R_{ct} , b) R_{pore} , c) C_{dl} , d) C_{film} .

the 5 nm ALD layer were lost in the first hours of immersion as confirmed by the disappearance of C_{film} and R_{pore} . The appearance of C_{dl} and R_{ct} indicates the onset of corrosion of the substrate. Their values can be compared to those of the bare substrate and be an indication of the active area on coated samples. At the end of the experiment the R_{ct} of the coated samples with 15 nm and 50 nm ALD layers were close to the R_{ct} of the bare alloy, implying a poor effect against the corrosion of the substrate. At the same time the samples were visually inspected (Fig. 11). The bare substrate was widely attacked. On the contrary, in the sample with 5 nm ALD film the corroded area was small and in the samples with thicker films corrosion it was practically absent. Despite the decrease in impedance, the visual inspection did not find noticeable signs of corrosion in the samples with 15 nm and 50 nm films. This is a

sign of the sensitivity of the EIS measurement. Time is needed to produce degradation and corrosion products in amount enough to be detectable by visual inspection.

3.5. Scanning vibrating electrode technique (SVET)

SVET measurements were performed to study with local resolution the electrochemical response of the samples after the EIS testing. The studied areas are identified with squares in Fig. 11. The results are presented in Fig. 12, where a)–c) correspond to areas A–C in Fig. 11. The SVET microelectrode scanned a plane 100 μm above the surface and measured the ionic currents associated with the electrochemical processes occurring at the surface [40]. The resulting maps show anodic

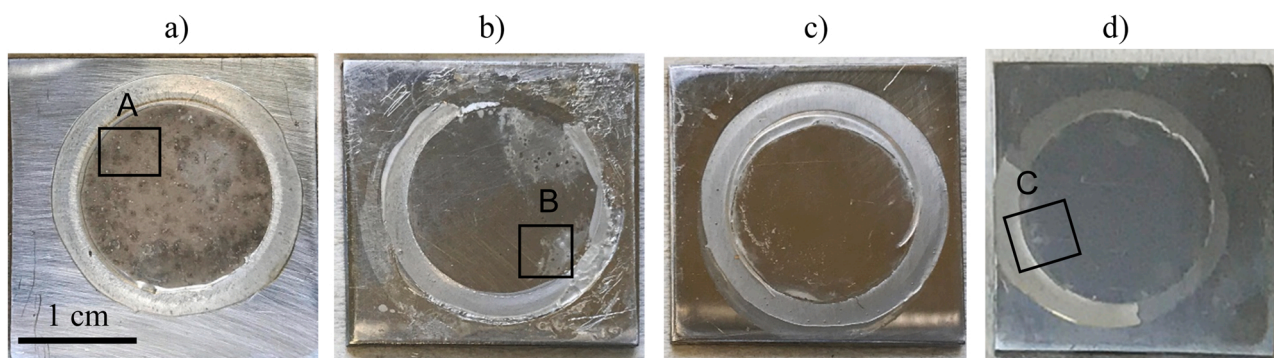


Fig. 11. Samples after EIS testing (48 h in 0.05 M NaCl): a) bare AA2024-T3 and AA2024-T3 coated by ALD layer with thicknesses of b) 5, c) 15 or d) 50 nm. The rectangles indicate the areas analysed by SVET.

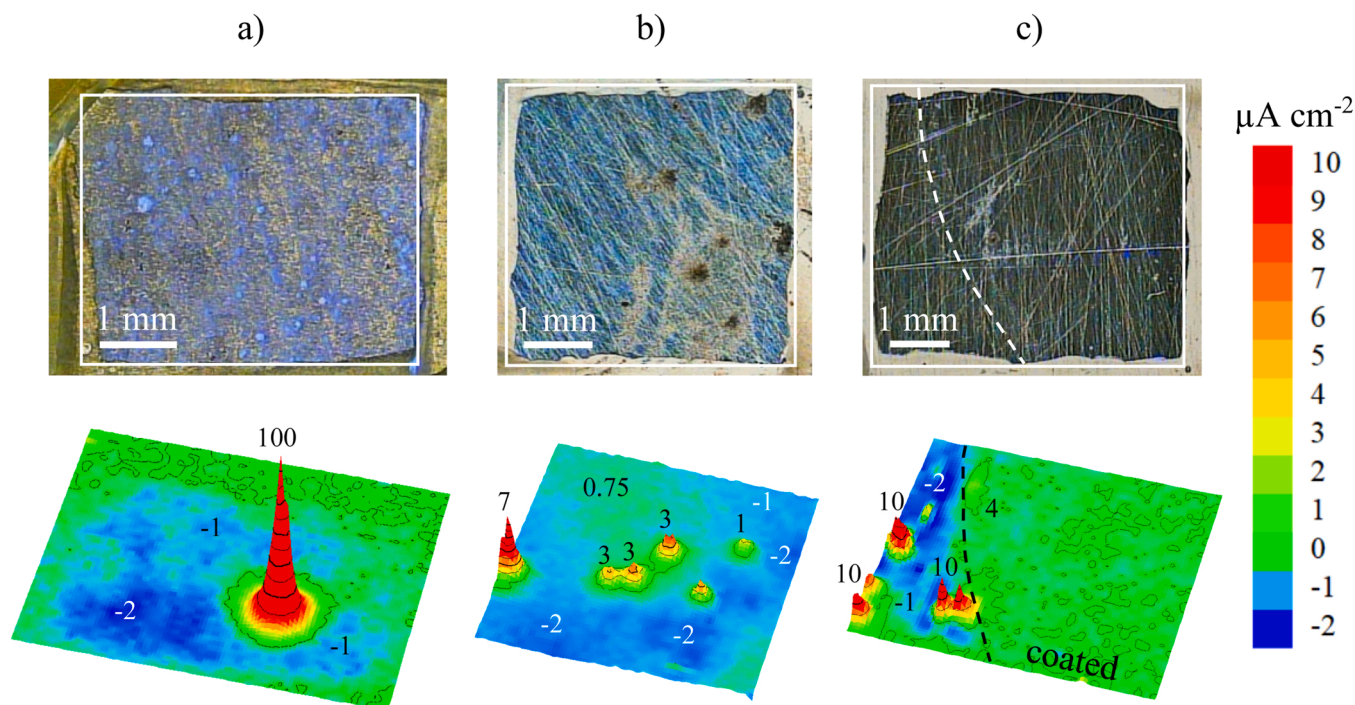


Fig. 12. Optical pictures and SVET current density maps ($\mu\text{A cm}^{-2}$) of tested areas after EIS measurement (48 h in 0.05 M NaCl): a) bare AA2024-T3, b) AA2024-T3 with 5 nm ALD layer and c) with 50 nm ALD layer. The white lines in the pictures indicate the scanned areas.

currents (positive, in red, resulting from the metal oxidation) and cathodic currents (negative, in blue, coming from the reduction reactions at the metal surface, typically oxygen reduction and/or hydrogen evolution from water reduction). The green colour in the maps indicates regions without measurable current (it includes situations where anodic and cathodic currents have the same magnitude and cancel out, and cases of current flowing in a direction normal to the vibration and therefore not measured).

The map of the bare substrate – Fig. 12 a) – presented net cathodic activity in most of the surface and one intense localized anodic spot. The sample coated with 5 nm ALD layer – Fig. 12 b) – showed a few anodic sites with low currents. This indicates the breakdown of the ALD layer, leaving active points ready for reaction compared to the barrier effect of the deposited corrosion products on the uncoated sample. It is important to note that the map in 12 b) was acquired in the region of the 5 nm sample with visible pits, i.e., the remaining area was not so active. The lowest currents were measured on the sample with the 50 nm ALD layer – Fig. 12 c). The analysed area is presented in Fig. 11 d) and was chosen to include a part exposed to solution during the EIS measurements and a smaller part that was beneath the PMMA tube used for delimiting the tested area. The epoxy glue used to attach the PMMA tube removed the ALD film, leaving exposed the AA2024-T3 substrate. The border between the two regions is identified by a dashed line in Fig. 12 c). The SVET map displays the different response of the bare substrate and of the ALD coated part. The corrosion activity was higher in the uncoated region and minor in the part coated with ALD, where local currents in the order of 1–2 $\mu\text{A cm}^{-2}$ were measured. It should be noted the absence of reduction reactions on the ALD coated part, which is in line with the fact that Al_2O_3 is usually electrochemically inert, and highly resistive to both electrons and ions (electronic and ionic currents). The map shows that the ALD film prevents the cathodic activity that could (if electron conductive) take place to feed the metal oxidation occurring in the uncoated region. The same resistance to the occurrence of electrochemical reactions was shown by the polarization curves in Fig. 6. Electrochemical reactions can only proceed in defects and pores of the ALD film.

The results obtained in this work confirm the deposition of alumina

films on AA2024-T3 by atomic layer deposition. The 5 nm film offered poor protection, which is agreement with previous reports that films with thickness lower than 10 nm present significant porosity [23,27, 29]. The films with thicknesses of 15 and 50 nm presented very low currents and exceptionally high impedances at the beginning of exposure to NaCl. However, the protection they provided faded in a few days. This has been reported before. Díaz et al. [56] worked with 50 nm thick Al_2O_3 layers grown by ALD at 160 °C on carbon steel and observed excellent sealing properties. However, the Al_2O_3 layer was unable to grant durable corrosion protection to the substrate, confirmed by a drop in the impedance over time. Similarly, Daubert et al. verified that Al_2O_3 films on copper provided high initial corrosion resistance, but the quality of the film degraded over time and ceased protecting the substrate from corrosion.

The explanation can be found in the literature: the Al_2O_3 films produced by ALD, particularly those at low temperature, are very sensitive to water attack. Nehm et al. using X-ray reflectivity observed a strong decrease in the Al_2O_3 film density after only 5 min storage in a 38 °C, and 90 % relative humidity environment [57]. Ellipsometer measurements revealed that Al_2O_3 films with a thickness of ~ 200 Å dissolved in water at 90 °C in ~ 10 days [28]. Díaz, in the work referred above [57], measured a dissolution rate of 7 nm/h of the ALD film in 0.2 M NaCl. Instead of dissolution under full water immersion, Garcia et al. [58] observed the conversion of the Al_2O_3 layer into hydroxides in a 85 °C/85 % RH environment. In their own words, crystalline Al_2O_3 (corundum) and high content (> 99 %) alumina ceramics are hydrothermally stable even at $T > 300$ °C [59,60]. Therefore, water does not corrode high purity crystalline Al_2O_3 . However, thin films grown at $T = 100$ °C by atomic layer deposition are amorphous with significant H-incorporation [32,61]. For growth at 100 °C, the H content is ~ 15 at %, increasing to > 20 % as the growth temperature is reduced to 50 °C. As a consequence, the chemical composition of those films is more accurately described as an oxy-hydroxide, $\text{AlO}_x(\text{OH})_{3-2x}$. In a 50 nm thick Al_2O_3 film grown on Si at 100 °C that was aged at 85 °C/85 % RH for 2 weeks, Garcia et al. identified by X-ray diffraction $\text{AlO}(\text{OH})$ and $\text{Al}(\text{OH})_3$ crystalline phases. They proposed that for the Al_2O_3 film deposited by ALD at lower temperatures the film composition is an

oxy-hydroxide and that this lowers the barrier energy for reaction with water facilitating the conversion of the amorphous Al_2O_3 thin films to hydroxide phases.

The simplest way to overcome the water sensitivity of the Al_2O_3 layers produced by ALD seems to be the deposition at higher temperature [32,57,58]. When the substrate does not allow it, some authors opted for depositing a more resistant layer, like TiO_2 or ZrO_2 , on the top of Al_2O_3 [28,57,58]. Another alternative worth trying is to replace H_2O for another precursor of oxygen during the atomic layer deposition of Al_2O_3 films.

4. Conclusions

Thin films of Al_2O_3 were applied on a heterogeneous metal surface like AA2024-T3 by atomic layer deposition (ALD) at low temperature (100 °C). The films were uniformly deposited over both aluminium matrix and intermetallic particles without visually identifiable defects. The 5 nm film was porous and did not provide good protection. The films with 15 nm and 50 nm thickness provided strong isolation of the surface with high impedance capacitive films. However, the protection was lost in the first days of immersion. This has been explained by the low temperature deposition process which introduced H-containing species in the film making it vulnerable to water.

CRediT authorship contribution statement

Marco Oliveira: Conceptualization, Methodology, Investigation, Formal analysis, Writing – original draft. Ricardo Silva: Methodology, Investigation, Writing – review & editing. Kiryl Yasakau: Methodology, Investigation, Formal analysis, Writing – review & editing. Alexandre Bastos: Conceptualization, Methodology, Supervision, Writing – review & editing. Silvar Kallip: Supervision, Writing – review & editing. Mikhail Zheludkevich: Supervision, Writing – review & editing. Rui Silva: Resources, Writing – review & editing. Mário Ferreira: Supervision, Resources, Writing – review & editing.

Declaration of Competing Interest

The authors declare that they have no known competing financial interests or personal relationships that could have appeared to influence the work reported in this paper.

Data Availability

Data will be made available on request.

Acknowledgements

Part of this work was developed within the scope of the project CICECO-Aveiro Institute of Materials, UIDB/50011/2020, UIDP/50011/2020, financed by national funds through the FCT/MEC (PIDDAC). MPO thanks FCT for financial support (SFRH/BD/117518/2016). KY acknowledges the Portuguese Foundation for Science and Technology for the researcher grant (IF/01284/2015). ACB is funded by national funds (OE), through FCT - Fundação para a Ciência e a Tecnologia, I.P., in the scope of the framework contract foreseen in the numbers 4, 5 and 6 of the article 23, of the Decree-Law 57/2016, of August 29, changed by Law 57/2017, of July 19. SK thanks ERA.NET for project RUS_ST2017-477 “ACTICOAT” and MSCA-RISE 2020 for Grant no. 101007430 “COAT4LIFE”.

Appendix A. Supporting information

Supplementary data associated with this article can be found in the online version at [doi:10.1016/j.corsci.2022.110773](https://doi.org/10.1016/j.corsci.2022.110773).

References

- [1] J.R. Davis, Corrosion of Aluminum and Aluminum Alloys, ASM International, 1999, <https://doi.org/10.31399/asm.tb.caaa.9781627082990>.
- [2] E. McCafferty, J.P. Wightman, Determination of the concentration of surface hydroxyl groups on metal oxide films by a quantitative XPS method, *Surf. Interface Anal.* 26 (1998) 549–564, doi: 10.1002/(SICI)1096-9918(199807)26:8<549::AID-SIA396>3.0.CO;2-Q.
- [3] J.R. Davis, ASM Specialty Handbook: Aluminum and Aluminum Alloys, ASM International, 1993. (http://www.asminternational.org/home/-/journal_content/56/10192/06610G/PUBLICATION/).
- [4] E.A. Starke, J.T. Staley, Application of modern aluminum alloy to aircraft, *Prog. Aerosp. Sci.* 32 (1996) 131–172, [https://doi.org/10.1016/0376-0421\(95\)00004-6](https://doi.org/10.1016/0376-0421(95)00004-6).
- [5] X. Chen, C.D. Marioara, S.J. Andersen, J. Friis, A. Lervik, R. Holmestad, E. Kobayashi, Precipitation processes and structural evolutions of various GPB zones and two types of S phases in a cold-rolled Al-Mg-Cu alloy, *Mater. Des.* 199 (2021), 109425, <https://doi.org/10.1016/j.matdes.2020.109425>.
- [6] V.A. Esin, L. Briez, M. Sennour, A. Koster, E. Gratiot, J. Crépin, Precipitation-hardness map for Al-Cu-Mg alloy (AA2024-T3), *J. Alloy. Compd.* 854 (2021), 157164, <https://doi.org/10.1016/j.jallcom.2020.157164>.
- [7] A.E. Hughes, R. Parvizi, M. Forsyth, Microstructure and corrosion of AA2024, *Corros. Rev.* 33 (2015) 1–30, <https://doi.org/10.1515/corrrev-2014-0039>.
- [8] N. Birbilis, B. Hinton, Corrosion and corrosion protection of aluminium, in: R. Lumley (Ed.), *Fundam. Alum. Metall.*, Elsevier, 2011, pp. 574–604, <https://doi.org/10.1533/9780857090256.2.574>.
- [9] F. Cui, F.J. Presuel-Moreno, R.G. Kelly, Experimental and computational evaluation of the protection provided by an aluminum cladding to AA2024-T3 exposed at a seacoast environment, *Corrosion* 62 (2006) 251–263, <https://doi.org/10.5006/1.3278271>.
- [10] C. Mitterer, PVD and CVD hard coatings, in: *Compr. Hard Mater.*, Elsevier, 2014, pp. 449–467, <https://doi.org/10.1016/B978-0-08-096527-7.00035-0>.
- [11] Z. Hsain, G. Zeng, N.C. Strandwitz, B.A. Krick, Wear behavior of annealed atomic layer deposited alumina, *Wear* 372–373 (2017) 139–144, <https://doi.org/10.1016/j.wear.2016.12.011>.
- [12] R.W. Johnson, A. Hultqvist, S.F. Bent, A brief review of atomic layer deposition: from fundamentals to applications, *Mater. Today* 17 (2014) 236–246, <https://doi.org/10.1016/j.mattod.2014.04.026>.
- [13] C. Marichy, M. Bechelany, N. Pinna, Atomic layer deposition of nanostructured materials for energy and environmental applications, *Adv. Mater.* 24 (2012) 1017–1032, <https://doi.org/10.1002/adma.201104129>.
- [14] K.J. Kuhn, Considerations for ultimate CMOS scaling, *IEEE Trans. Electron. Devices* 59 (2012) 1813–1828, <https://doi.org/10.1109/TED.2012.2193129>.
- [15] D. Beckel, A. Bieberle-Hütter, A. Harvey, A. Infourtuna, U.P. Muecke, M. Prestat, J.L. M. Rupp, L.J. Gauckler, Thin films for micro solid oxide fuel cells, *J. Power Sources* 173 (2007) 325–345, <https://doi.org/10.1016/j.jpowsour.2007.04.070>.
- [16] L. Fernández-Menéndez, A. González, V. Vega, V. de la Prida, Electrostatic supercapacitors by atomic layer deposition on nanoporous anodic alumina templates for environmentally sustainable energy storage, *Coatings* 8 (2018) 403, <https://doi.org/10.3390/coatings8110403>.
- [17] J.R. Bakke, K.L. Pickrahn, T.P. Brennan, S.F. Bent, Nanoengineering and interfacial engineering of photovoltaics by atomic layer deposition, *Nanoscale* 3 (2011) 3482, <https://doi.org/10.1039/c1nr10349k>.
- [18] X. Meng, X. Wang, D. Geng, C. Ozgit-Akgun, N. Schneider, J.W. Elam, Atomic layer deposition for nanomaterial synthesis and functionalization in energy technology, *Mater. Horiz.* 4 (2017) 133–154, <https://doi.org/10.1039/C6MH00521G>.
- [19] X. Wang, G. Yushin, Chemical vapor deposition and atomic layer deposition for advanced lithium ion batteries and supercapacitors, *Energy Environ. Sci.* 8 (2015) 1889–1904, <https://doi.org/10.1039/C5EE01254F>.
- [20] B.J. O'Neill, D.H.K.K. Jackson, J. Lee, C. Canlas, P.C. Stair, C.L. Marshall, J. W. Elam, T.F. Kuech, J.A. Dumesic, G.W. Huber, Catalyst design with atomic layer deposition, *ACS Catal.* 5 (2015) 1804–1825, <https://doi.org/10.1021/cs501862h>.
- [21] N.K.R. Eswar, S.A. Singh, J. Heo, Atomic layer deposited photocatalysts: comprehensive review on viable fabrication routes and reactor design approaches for photo-mediated redox reactions, *J. Mater. Chem. A* 7 (2019) 17703–17734, <https://doi.org/10.1039/C9TA04780H>.
- [22] Y.J. Pagán-Torres, J.M.R. Gallo, D. Wang, H.N. Pham, J.A. Libera, C.L. Marshall, J. W. Elam, A.K. Datye, J.A. Dumesic, Synthesis of highly ordered hydrothermally stable mesoporous niobia catalysts by atomic layer deposition, *ACS Catal.* 1 (2011) 1234–1245, <https://doi.org/10.1021/cs200367t>.
- [23] B. Díaz, E. Härkönen, J. Świątowska, V. Maurice, A. Seyeux, P. Marcus, M. Ritala, Low-temperature atomic layer deposition of Al_2O_3 thin coatings for corrosion protection of steel: surface and electrochemical analysis, *Corros. Sci.* 53 (2011) 2168–2175, <https://doi.org/10.1016/j.corsci.2011.02.036>.
- [24] B. Díaz, J. Świątowska, V. Maurice, A. Seyeux, E. Härkönen, M. Ritala, S. Tervakangas, J. Kolehmainen, P. Marcus, Tantalum oxide nanocoatings prepared by atomic layer and filtered cathodic arc deposition for corrosion protection of steel: comparative surface and electrochemical analysis, *Electrochim. Acta* 90 (2013) 232–245, <https://doi.org/10.1016/j.electacta.2012.12.007>.
- [25] E. Härkönen, S. Tervakangas, J. Kolehmainen, B. Díaz, J. Świątowska, V. Maurice, A. Seyeux, P. Marcus, M. Fenker, L. Tóth, G. Radnóci, M. Ritala, Interface control of atomic layer deposited oxide coatings by filtered cathodic arc deposited sublayers for improved corrosion protection, *Mater. Chem. Phys.* 147 (2014) 895–907, <https://doi.org/10.1016/j.matchemphys.2014.06.035>.
- [26] M. Fedel, F. Defforian, Electrochemical characterization of atomic layer deposited Al_2O_3 coatings on AISI 316L stainless steel, *Electrochim. Acta* 203 (2016) 404–415, <https://doi.org/10.1016/j.electacta.2016.02.107>.

- [27] B. Díaz, J. Świątowska, V. Maurice, A. Seyeux, B. Normand, E. Härkönen, M. Ritala, P. Marcus, Electrochemical and time-of-flight secondary ion mass spectrometry analysis of ultra-thin metal oxide (Al_2O_3 and Ta_2O_5) coatings deposited by atomic layer deposition on stainless steel, *Electrochim. Acta* 56 (2011) 10516–10523, <https://doi.org/10.1016/j.electacta.2011.02.074>.
- [28] A.I. Abdulagatov, Y. Yan, J.R. Cooper, Y. Zhang, Z.M. Gibbs, A.S. Cavanagh, R. G. Yang, Y.C. Lee, S.M. George, Al_2O_3 and TiO_2 atomic layer deposition on copper for water corrosion resistance, *ACS Appl. Mater. Interfaces* 3 (2011) 4593–4601, <https://doi.org/10.1021/am2009579>.
- [29] J.S. Daubert, G.T. Hill, H.N. Gotsch, A.P. Gremaud, J.S. Ovental, P.S. Williams, C. J. Oldham, G.N. Parsons, Corrosion protection of copper using Al_2O_3 , TiO_2 , ZnO , HfO_2 , and ZrO_2 atomic layer deposition, *ACS Appl. Mater. Interfaces* 9 (2017) 4192–4201, <https://doi.org/10.1021/acsami.6b13571>.
- [30] M. Merisalu, L. Aarik, J. Kozlova, H. Mändar, A. Tarre, V. Sammelselg, Effective corrosion protection of aluminum alloy AA2024-T3 with novel thin nanostructured oxide coating, *Surf. Coat. Technol.* 411 (2021), 126993, <https://doi.org/10.1016/j.surfcoat.2021.126993>.
- [31] S.M. George, Atomic layer deposition: an overview, *Chem. Rev.* 110 (2010) 111–131, <https://doi.org/10.1021/cr900056b>.
- [32] M.D. Groner, F.H. Fabreguette, J.W. Elam, S.M. George, Low-temperature Al_2O_3 atomic layer deposition, *Chem. Mater.* 16 (2004) 639–645, <https://doi.org/10.1021/cm0304546>.
- [33] L. Wang, M. Strangwood, D. Balint, J. Lin, T.A. Dean, Formability and failure mechanisms of AA2024 under hot forming conditions, *Mater. Sci. Eng. A* 528 (2011) 2648–2656, <https://doi.org/10.1016/j.msea.2010.11.084>.
- [34] A. Lipski, S. Mroziński, The effects of temperature on the strength properties of aluminium alloy 2024-T3, *Acta Mech. Autom.* 6 (2012) 62–66.
- [35] K. Yasakau, Application of AFM-based techniques in studies of corrosion and corrosion inhibition of metallic alloys, *Corros. Mater. Degrad.* 1 (2020) 345–372, <https://doi.org/10.3390/cmd1030017>.
- [36] C. Örnek, C. Leygraf, J. Pan, On the Volta potential measured by SKPFM – fundamental and practical aspects with relevance to corrosion science, *Corros. Eng. Sci. Technol.* 54 (2019) 185–198, <https://doi.org/10.1080/1478422X.2019.1583436>.
- [37] M. Rohwerder, F. Turcu, High-resolution Kelvin probe microscopy in corrosion science: scanning Kelvin probe force microscopy (SKPFM) versus classical scanning Kelvin probe (SKP), *Electrochim. Acta* 53 (2007) 290–299, <https://doi.org/10.1016/j.electacta.2007.03.016>.
- [38] H.O. Jacobs, H.F. Knapp, S. Müller, A. Stemmer, Surface potential mapping: a qualitative material contrast in SPM, *Ultramicroscopy* 69 (1997) 39–49, [https://doi.org/10.1016/S0304-3991\(97\)00027-2](https://doi.org/10.1016/S0304-3991(97)00027-2).
- [39] H.O. Jacobs, P. Leuchtmann, O.J. Homan, A. Stemmer, Resolution and contrast in Kelvin probe force microscopy, *J. Appl. Phys.* 84 (1998) 1168–1173, <https://doi.org/10.1063/1.368181>.
- [40] A.C. Bastos, M.C. Quevedo, O.V. Karavai, M.G.S. Ferreira, Review—on the application of the scanning vibrating electrode technique (SVET) to corrosion research, *J. Electrochem. Soc.* 164 (2017), <https://doi.org/10.1149/2.043171jes>.
- [41] applicableelectronics, n.d. (www.applicableelectronics.com), (Accessed 10 January 2019).
- [42] Science Wares Inc., n.d. (www.sciencewares.com), (Accessed 10 January 2019).
- [43] Microprobes for Life Science, n.d. (<https://www.microprobes.com/>), (Accessed 10 January 2019).
- [44] A. Boag, A.E. Hughes, A.M. Glenn, T.H. Muster, D. McCulloch, Corrosion of AA2024-T3 Part I: localised corrosion of isolated IM particles, *Corros. Sci.* 53 (2011) 17–26, <https://doi.org/10.1016/j.corsci.2010.09.009>.
- [45] S. Mirhashemihaghighi, J. Świątowska, V. Maurice, A. Seyeux, L.H. Klein, E. Salmi, M. Ritala, P. Marcus, The role of surface preparation in corrosion protection of copper with nanometer-thick ALD alumina coatings, *Appl. Surf. Sci.* 387 (2016) 1054–1061, <https://doi.org/10.1016/j.apsusc.2016.06.188>.
- [46] A. Jaggermuth, R.M. Silva, M.A. Neto, F.J. Oliveira, I.K. Bdkin, M.P. Alegre, M. Gutiérrez, D. Araújo, J.C. Mendes, R.F. Silva, Interfacial integrity enhancement of atomic layer deposited alumina on boron doped diamond by surface plasma functionalization, *Surf. Coat. Technol.* 397 (2020), 125991, <https://doi.org/10.1016/j.surfcoat.2020.125991>.
- [47] Maria J. Lima, Ricardo M. Silva, Kira Gonzalez, José D. Castro, Filipe Oliveira, Rui F. Silva, Sandra Carvalho, Modification of steel surfaces with nanometer films of Al_2O_3 and TiO_2 decreases interfacial adhesion to polymers: implications for demolding shape-engineered polymer products, *ACS Appl. Nano Mater.* 4 (2021) 10018–10028, <https://doi.org/10.1021/acsnam.1c00995>.
- [48] K.A. Yasakau, M.L. Zheludkevich, O.V. Karavai, M.G.S. Ferreira, Influence of inhibitor addition on the corrosion protection performance of sol-gel coatings on AA2024, *Prog. Org. Coat.* 63 (2008) 352–361, <https://doi.org/10.1016/j.porgcoat.2007.12.002>.
- [49] P. Schmutz, G.S. Frankel, Characterization of AA2024-T3 by scanning Kelvin probe force microscopy, *J. Electrochem. Soc.* 145 (1998) 2285–2295, <https://doi.org/10.1149/1.1838633>.
- [50] K.A. Yasakau, A.N. Salak, M.L. Zheludkevich, M.G.S.S. Ferreira, Volta potential of oxidized aluminum studied by scanning Kelvin probe force microscopy, *J. Phys. Chem. C* 114 (2010) 8474–8484, <https://doi.org/10.1021/jp1011044>.
- [51] G. Grundmeier, K.M. Juttner, M. Stratmann, Corrosion and environmental degradation, Volumes I–II, *Anti-Corros. Methods Mater.* 47 (2000) 43–46, <https://doi.org/10.1108/acmm.2000.12847fae.001>.
- [52] M. Mibus, C. Jensen, X. Hu, C. Knosp, M.L. Reed, G. Zangari, Dielectric breakdown and failure of anodic aluminum oxide films for electrowetting systems, *J. Appl. Phys.* 114 (2013), 014901, <https://doi.org/10.1063/1.4812395>.
- [53] H. Shi, E.-H. Han, F. Liu, Corrosion protection of aluminium alloy 2024-T3 in 0.05 M NaCl by cerium cinnamate, *Corros. Sci.* 53 (2011) 2374–2384, <https://doi.org/10.1016/j.corsci.2011.03.012>.
- [54] M.E. Orazem, B. Tribollet, *Electrochemical Impedance Spectroscopy*, Wiley, 2008, <https://doi.org/10.1002/9780470381588>.
- [55] G.J. Brug, A.L.G. van den Eeden, M. Sluyters-Rehbach, J.H. Sluyters, The analysis of electrode impedances complicated by the presence of a constant phase element, *J. Electroanal. Chem. Interfacial Electrochem* 176 (1984) 275–295, [https://doi.org/10.1016/S0022-0728\(84\)80324-1](https://doi.org/10.1016/S0022-0728(84)80324-1).
- [56] B. Díaz, E. Härkönen, V. Maurice, J. Świątowska, A. Seyeux, M. Ritala, P. Marcus, Failure mechanism of thin Al_2O_3 coatings grown by atomic layer deposition for corrosion protection of carbon steel, *Electrochim. Acta* 56 (2011) 9609–9618, <https://doi.org/10.1016/j.electacta.2011.07.104>.
- [57] F. Nehm, H. Klumbies, C. Richter, A. Singh, U. Schroeder, T. Mikolajick, T. Mönch, C. Hoßbach, M. Albert, J.W. Bartha, K. Leo, L. Müller-Meskamp, Breakdown and protection of ALD moisture barrier thin films, *ACS Appl. Mater. Interfaces* 7 (2015) 22121–22127, <https://doi.org/10.1021/acsami.5b06891>.
- [58] P.F. Garcia, R.S. McLean, Z.G. Li, M.H. Reilly, W.J. Marshall, Permeability and corrosion in $\text{ZrO}_2/\text{Al}_2\text{O}_3$ nanolaminate and Al_2O_3 thin films grown by atomic layer deposition on polymers, *J. Vac. Sci. Technol. A* 30 (2012) 41515, <https://doi.org/10.1116/1.4729447>.
- [59] X.-M. Yue, G.-J. Zhang, T. Watanabe, W.-P. Tai, Corrosion behavior of single-crystal alumina in argon, air, and water vapor atmospheres at 1700–2000 °C, *J. Am. Ceram. Soc.* 82 (1999) 2560–2562, <https://doi.org/10.1111/j.1151-2916.1999.tb02122.x>.
- [60] K. Oda, T. Yoshio, Hydrothermal corrosion of alumina ceramics, *J. Am. Ceram. Soc.* 80 (1997) 3233–3236, <https://doi.org/10.1111/j.1151-2916.1997.tb03258.x>.
- [61] V. Verlaan, L.R.J.G. van den Elzen, G. Dingemans, M.C.M. van de Sanden, W.M. M. Kessels, Composition and bonding structure of plasma-assisted ALD Al_2O_3 films, *Phys. Status Solidi C* 7 (2010) 976–979, <https://doi.org/10.1002/pssc.200982891>.